Hindawi
International Journal of Energy Research
Volume 2024, Article ID 4459617, 13 pages
https://doi.org/10.1155/2024/4459617

Research Article

Oxygen Vacancy-Rich $NiCo_2O_4$ on Carbon Framework with Controlled Pore Architectures as Efficient Bifunctional Electrocatalysts for Zn-Air Batteries

Min Kim,[1] Jeong Hoo Hong,[1] Ki Beom Kim,[1] Hye Young Koo,[2] and Yun Chan Kang[1]

[1]*Department of Materials Science and Engineering, Korea University, Anam-dong, Seongbuk-gu, Seoul 136-713, Republic of Korea*
[2]*Department of Metal Powder, Korea Institute of Materials Science, 797 Changwon-daero, Changwon, Gyeongnam 51508, Republic of Korea*

Correspondence should be addressed to Hye Young Koo; hykoo@kims.re.kr and Yun Chan Kang; yckang@korea.ac.kr

Received 12 February 2024; Revised 15 April 2024; Accepted 2 May 2024; Published 16 May 2024

Academic Editor: Ahmad Azmin Mohamad

Transition metal oxides are considered alternative electrocatalysts for ZAB owing to their multiple oxidation states. However, they have limitations such as low electrical conductivity and the deficiency of reactive sites. In this study, to overcome these shortcomings and improve electrocatalytic activity, oxygen vacancies and porous architectures were introduced through a partial reduction process and a porous carbon framework. Open porous carbon microspheres with uniformly loaded $NiCo_2O_4$ nanosheets and oxygen vacancies (V-NCO/OPC) displayed enhanced electrocatalytic performance with a low Tafel slope (68 mV dec^{-1}) in the oxygen reduction reaction (ORR) and a low overpotential (402 mV) at 10 mA cm^{-2} in the oxygen evolution reaction (OER). The combined effect of the oxygen vacancies and porous architecture can offer sufficient active sites, modify the electronic structure of the metal oxide surface, and facilitate mass transport, enhancing the electrocatalytic properties of V-NCO/OPC. Furthermore, when applied for ZAB, V-NCO/OPC demonstrated better electrochemical performance including discharge power density (154.9 mW cm^{-2}) at the current density of 175.9 mA cm^{-2}, low voltage gap (0.85 V) at the initial cycle, and long-term (250 h) cycle stability at the current density of 10 mA cm^{-2} than those of noble-metal electrocatalysts.

1. Introduction

Rechargeable zinc-air batteries (ZABs) are considered one of the most sustainable battery technologies owing to their characteristics such as high theoretical energy density (1086 W h kg^{-1}), low cost, and safe operation [1–4]. Especially, ZABs are inherently ecofriendly due to their utilization of nontoxic zinc as the anode material, their potential recyclability, and the availability of aqueous electrolytes. Owing to the sluggish oxygen catalytic kinetics, the catalytic activity of the cathode material in the oxygen reduction reaction (ORR) and oxygen evolution reaction (OER) plays a crucial role in the remarkable performance of ZABs [5–8]. Noble metal-based materials such as Pt and IrO_2/RuO_2 are well-known catalysts with superior ORR and OER catalytic activities, respectively [9–11]. However, the conflict between the increasing energy demand and limited resource supply caused by the low natural abundance of noble metals limits the large-scale applications of these materials [12–18]. In addition, their poor durability, caused by the deformation of the nanoparticles during the electrochemical process, brings about the deactivation of the catalyst [19–21]. Therefore, the development of noble-metal-free bifunctional electrocatalysts possessing high activity and durability at a low cost is important for achieving extensive practical applications [22, 23].

Transition metal oxides (TMOs) have attracted considerable interest as bifunctional electrocatalysts owing to their low cost and multiple oxidation states from their unique crystal structure [22, 24–26]. However, their deficiency in reactive sites and intrinsically inferior electrical conductivity remain challenging [27–30]. Employing oxygen vacancies in

the transition metal oxide lattice has been reported as an effective strategy for addressing the issues [31, 32]. Oxygen vacancies in the lattice of the metal oxide modify the electronic structure, which not only forms several active sites for adsorption but also enhances electrical conductivity [33, 34]. Utilizing a carbon framework with a porous architecture is another important strategy for boosting the electrocatalytic activity of transition metal oxides [35–38]. Pore size modulation, including micro-, meso-, and macropores, can facilitate the electrocatalytic activity by regulating the crystal size to expose sufficient active sites, promote mass transport, and facilitate the detachment of the O_2 bubble-blocking surface of the active site [8, 39–41]. Among the various TMOs, $NiCo_2O_4$ (NCO), which is a spinel oxide with Ni ions occupying octahedral sites in the Co_3O_4 lattice, has attracted significant attention as an electrocatalyst owing to its availability and stability [42–45]. Yuan et al. reported the superior ORR activity of NCO nanosheets on hollow mesoporous carbon with oxygen vacancies through an annealing treatment in a low-oxygen atmosphere [46]. Liu et al. explored ultrathin NCO nanosheets with oxygen vacancies as bifunctional zinc-air cathode materials synthesized under different calcination atmospheres [47].

Spray pyrolysis, which is a continuous reaction process possessing high efficiency, can be considered an effective synthetic process for porous carbon frameworks [48]. Moreover, the use of an aqueous solution containing various components and short-time synthesis for spray pyrolysis are very powerful factors for ecofriendliness and scalability. Various removable organic/inorganic materials contained in the droplets can be used to easily fabricate porous structures suitable for supporting transition metal compounds after spray pyrolysis. In this study, NCO with oxygen vacancies on three-dimensional (3D) open-pore-structured porous carbon microspheres (V-NCO/OPC) was prepared as a bifunctional electrocatalyst. The unique porous structure of the carbon framework provides a high surface area for uniform decoration of NCO nanosheets, as well as desired diffusion channels for electrolyte and oxygen. Moreover, with the accompanying morphological advantages, the oxygen vacancies created in NCO by the cost-effectiveness of the $NaBH_4$ reducing agent with water enhanced the electrocatalytic activity by changing the valence state and electronic structure within a short time. Consequently, V-NCO/OPC exhibited outstanding performance in the ORR and OER processes in alkaline media, as well as low polarization and long-term cycle stability in ZABs.

2. Experimental

MgO/open-pore-structured carbon composite microspheres (Mg-OPC) were synthesized by a one-pot spray pyrolysis process using a carbon source and a pore-forming agent. A spray solution was prepared by dissolving 0.1 M magnesium nitrate and 4 g of carbon sources composed of dextrin and polyvinylpyrrolidone (PVP; $M_w = 40{,}000$) in a weight ratio of 1 : 1, followed by dispersing 2 g of 100 nm polystyrene (PS) nanobeads in distilled water (200 mL). The colloidal solution was nebulized into droplets by an ultrasonic spray generator, and the droplets passed through a reactor maintained at 800°C with an N_2 gas flow rate of 10 L min^{-1}. Based on the synthesis through spray pyrolysis on a lab scale, approximately 1.3 g of powder can be obtained from a 1 L precursor solution. After the etching process using HCl solution to remove MgO particles and the subsequent carbonization process at 800°C under Ar gas flow for 3 h, 3D open-pore structured carbon microspheres (denoted as OPC) were obtained. To decorate NCO on the microspheres, 0.01 g of nickel acetate, 0.02 g of cobalt acetate, and 0.025 g of hexamethylenetetramine (HMTA) were dissolved in 50 mL of ethanol under continuous stirring and 0.02 g of OPC was added to the homogenous solution. The reaction mixture was transferred into a Teflon-lined autoclave and was treated at 110°C for over 16 h. The resultant precipitate was washed with DI water several times and calcined at 280°C for 2 h in the air to obtain the NCO nanosheets/OPC (NCO/OPC). Subsequently, the NCO/OPC was dispersed in a 0.025 M $NaBH_4$ aqueous solution for 45 min, resulting in V-NCO/OPC. For comparison, porous carbon microspheres without open macropores decorated with NCO nanosheets (denoted as NCO/PC) were synthesized using an identical procedure without PS nanobeads. MgO/PC composite microspheres prepared from the spray solution without PS nanobeads transformed into porous carbon microspheres (denoted as PC) without open macropores. Detailed information including characterization methods, ORR and OER measurements, and manufacture and measurement of the ZABs is described in supporting information.

3. Results and Discussion

A schematic illustration for synthesizing V-NCO/OPC is shown in Scheme 1. The spray pyrolysis process involves atomizing a spray solution into droplets using ultrasonic force, followed by their evaporation and decomposition in a heated reactor. When a droplet containing dextrin, PVP, Mg nitrate, and PS nanobeads passes through the reactor, which is exposed to high temperatures, solvent evaporation and decomposition for each component occur. This rapid process ensures the formation of aggregate-free spherical microspheres from each droplet, with particles spending only a short time in the reactor furnace. Then, the Mg nitrate and carbon sources (dextrin and PVP) were converted into MgO and carbon frameworks, respectively, and the PS nanobeads were decomposed into gas phases including CO_2 and H_2O to create macropores [49]. In this process, MgO nanocrystals act as inorganic catalysts that convert the carbon sources into a carbon framework [50]. The existence of MgO in Mg-OPC was demonstrated by the XRD pattern in Figure S1. The resultant microspheres were etched using a dilute HCl solution to eliminate MgO and complete the carbonization of the carbon framework with further heat treatment to form the OPC microspheres. NCO nanosheets were decorated on OPC via a hydrothermal method and subsequent oxidation. During the hydrothermal process, the Ni^{2+} and Co^{2+} ions, initially absorbed onto the surface of OPC, underwent a chemical transformation facilitated by the presence of OH^- ions generated through the hydrolysis

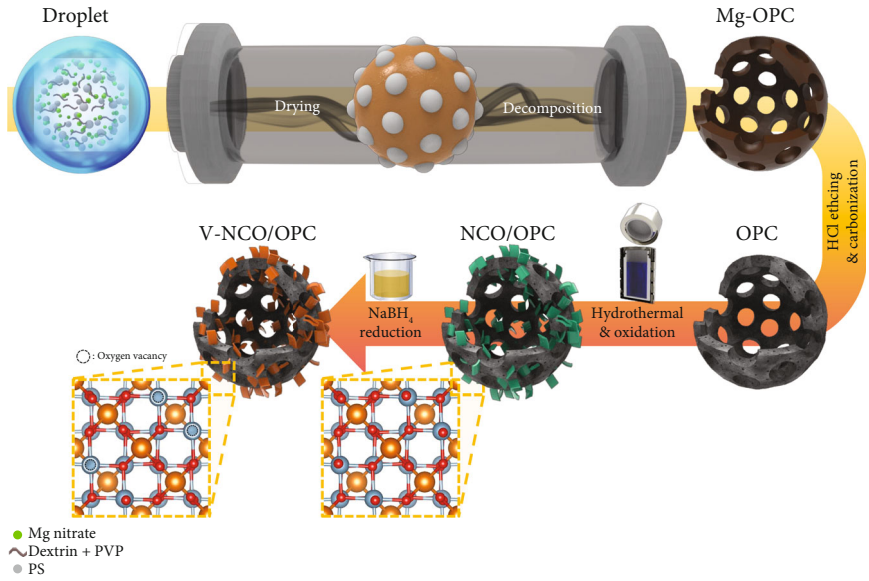

Scheme 1: Formation mechanism of V-NCO/OPC.

of HMTA. This led to the formation of $NiCo_2(OH)_6$ nanosheets, and the nanosheets were transformed into NCO nanosheets during an oxidation process. The overall reactions are conducted by following the chemical equations [51, 52].

$$\begin{aligned}(CH_2)_6N_4 + 6H_2O &\rightarrow 4NH_3 + 6HCHO\\ NH_3 + H_2O &\rightarrow NH^{4+} + OH^-\\ Ni^{2+} + 2Co^{2+} + 6OH^- &\rightarrow NiCo_2(OH)_6\\ NiCO_2(OH)_6 + 1/2O_2 &\rightarrow NiCo_2O_4 + 3H_2O\end{aligned} \quad (1)$$

Through reaction with $NaBH_4$ solution, oxygen vacancies are introduced into the NCO lattice by the abundant hydrogen gas generated by $NaBH_4$, which produces V-NCO/OPC.

The structural difference between OPC and porous carbon without open pores (PC) was compared using scanning electron microscopy (SEM) images in Figure 1. Numerous macropores generated by the decomposition of PS nanobeads in Mg-OPC and no visible morphological changes after etching to remove the MgO crystals in OPC were confirmed in Figures 1(a) and 1(b). In contrast, the MgO/PC composite microspheres exhibited no macropores owing to the absence of PS nanobeads in the spray solution, and PC possessed only pores formed by etching MgO (Figures 1(c) and 1(d)). To further compare the differences between OPC and PC, their surface areas and pore structures were analyzed. The isotherms shown in Figure S2(a) exhibit a typical type IV hysteresis, indicating that the samples had an abundance of micro/mesopores [53]. The BET surface areas of OPC and PC were 757.9 and 519.8 $m^2 g^{-1}$, respectively. The open-macroporous structure enhances the surface area of the OPC. The Barrett-Joyner-Halenda (BJH) pore size distributions of OPC and PC in Figure S2(b) revealed mesopores with a maximum peak of around 4.5 and 4.9 nm, respectively. The increased specific surface area of OPC with micro/mesopores can be considered as a more suitable carbon framework for not only decorating the NCO component but also encouraging the mass transfer of oxygen molecules and the electrolyte.

After the hydrothermal method and oxidation treatment, NCO nanosheets were successfully loaded onto OPC and PC, as confirmed by the X-ray diffraction (XRD) patterns shown in Figure S3. The morphologies of NCO/OPC and NCO/PC were investigated by SEM and transmission electron microscopy (TEM) in Figure 2 and Figure S4, respectively. Ultrafine NCO nanosheets were uniformly decorated on the surface of the OPC, and the open pore structure was maintained after NCO loading in Figures 2(a) and 2(b). However, in the case of NCO/PC, large NCO nanosheets were deposited on the surface of the PC (Figures S4(a) and S4(b)). The presence of macropores prevents the large growth of NCO nanosheets on the surface and allows NCO to be uniformly distributed in small sizes. From the high-resolution TEM (HR-TEM) image of NCO/OPC in Figure 2(c), the two lattice fringe spacings of 0.21 nm matching the (400) and (040) planes of the cubic structure were observed, which is in line with the results from the XRD pattern of NCO nanosheets (JCPDS 20-07810). The selected-area electron diffraction (SAED) pattern in Figure 2(d) also reveals well-defined diffraction rings in the (511), (400), (311), and (111) crystal planes of NCO. The uniform distributions of Co, Ni, O, and C on the OPC surface are demonstrated in the elemental mapping images in Figure 2(c). The HR-TEM and SAED patterns presented in Figures S4(c) and S4(d), respectively, demonstrated the successful decoration of PC with the NCO nanosheets.

The changes in the surface area and pore structure after NCO loading were analyzed using N_2 gas adsorption/desorption isotherms, and the corresponding results are shown in Figure S5. The hysteresis types of NCO/OPC and NCO/PC (Figure S5(a)) were identical to those of OPC

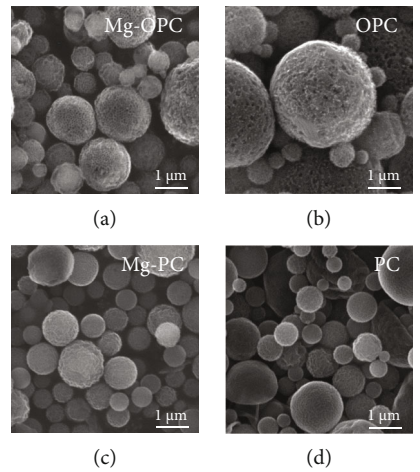

Figure 1: SEM images of (a) Mg-OPC, (b) OPC, (c) Mg-PC, and (d) PC.

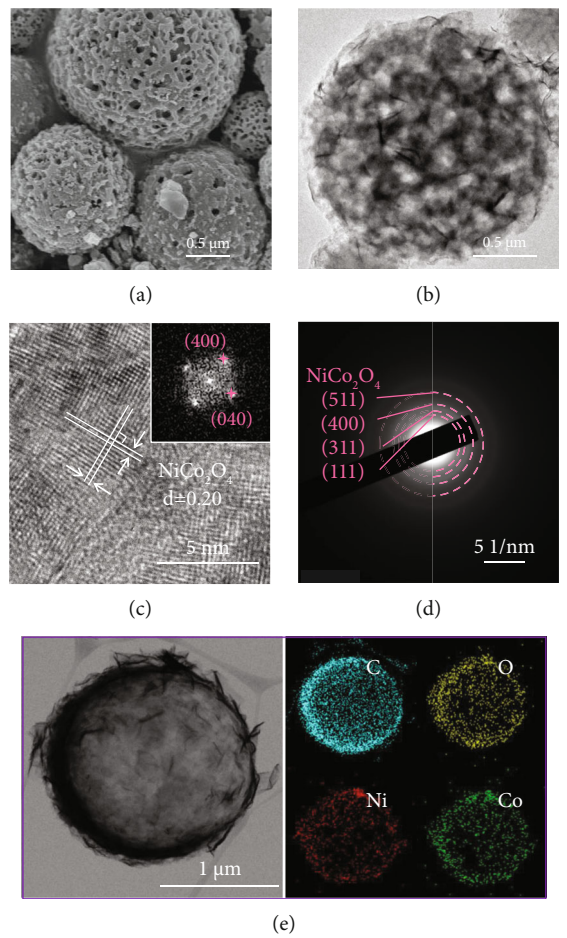

Figure 2: Morphologies, SAED pattern, and elemental mapping images of NCO/OPC: (a) SEM image, (b) TEM image, (c) HR-TEM image (insert: fast Fourier transform electron diffraction pattern), (d) SAED pattern, and (e) elemental mapping images.

and PC. However, the surface area of NCO/OPC decreased slightly to 718.5 $m^2 g^{-1}$, while that of NCO/PC decreased significantly to 353.2 $m^2 g^{-1}$. The macropores of NCO/OPC were not blocked even after the loading of NCO nanosheets, which also led to the inhibition of crystal growth to form ultrafine NCO nanosheets. However, the micro/mesopores of NCO/PC were blocked by large-sized NCO nanosheets owing to the absence of macropores; therefore, NCO/OPC exhibited a smaller decrease in surface area than NCO/PC. The Barrett-Joyner-Halenda (BJH) pore-size distribution in

Figure S5(b) showed a decrease in the volume fraction of pores less than 5 nm in NCO/OPC and NCO/PC compared to that in OPC and PC, which suggests the successful loading of NCO in the carbon framework. To determine the actual NCO content in the carbon framework, the thermogravimetric analysis (TGA) of NCO/OPC and NCO/PC was performed under an airflow from 25 to 800°C at a heating rate of 10°C min^{-1}, as shown in Figure S6. The initial weight loss below 150°C corresponded to the evaporation of water molecules that had been adsorbed on each sample. The subsequent dramatic drop occurring from 300 to 500°C was related to the combustion of the carbon framework. The TGA results confirmed that NCO/OPC and NCO/PC contained the same amount of $NiCo_2O_4$ (approximately 23 wt.%).

In general, the presence of oxygen vacancies in the lattice of metal oxide materials enhances their electrocatalytic performance in the ORR and OER. To introduce oxygen vacancies into the NCO/OPC, a partial reduction process using a $NaBH_4$ solution was conducted. The XRD pattern of V-NCO/OPC, as shown in Figure S7, exhibited no change in the crystal structure but showed lower peak intensities, indicating the creation of oxygen vacancies in the NCO lattice. The SEM image in Figure 3(a) demonstrated that, even after the chemical reduction step, the morphology of the sample was approximately intact without structural destruction, and the TEM image in Figure 3(b) confirmed that the shape of the NCO nanosheets was maintained after the formation of V-NCO. The HR-TEM image in Figure 3(c) also showed two clear lattice fringes at an angle of 90°, which suggests that the cubic crystal structure was well-maintained after the introduction of oxygen vacancies. The diffraction rings in the SAED pattern were also in agreement with the crystal planes of NCO in Figure 3(d). However, unlike the SAED pattern of NCO/OPC, some diffraction rings of NCO were not observed, which could be attributed to the decrease in crystallinity caused by the formation of oxygen vacancies.

To verify the formation of oxygen vacancies in the lattice of NCO, X-ray photoelectron spectroscopy (XPS) was performed, and all the spectra of NCO/OPC and V-NCO/OPC were compared. The survey scans of both samples, shown in Figure 4(a), indicate the presence of elements corresponding to NCO and carbon. The Co 2p spectrum (Figure 4(b)) was divided into four major peaks and two satellite peaks. Peaks related to Co^{3+}/Co^{2+} in Co $2p_{3/2}$ and Co $2p_{1/2}$ were located at 779.7/781.1 eV and 795.1/796.6 eV, respectively, and two satellite peaks were assigned to 785.8 and 802.3 eV [54]. In the Ni 2p spectrum, peaks corresponding to Ni^{3+}/Ni^{2+} were observed at 854.1/855.5 and 871.9/873.1 eV in the Ni $2p_{3/2}$ and Ni $2p_{1/2}$ orbitals, respectively, and satellite peaks were displayed at 861.1 and 879.2 eV (Figure 4(c) [55–57]. Three deconvoluted peaks located at 529.3, 531.6, and 533.4 eV in the O 1s spectrum corresponded to the lattice oxygen atoms, defect sites with oxygen vacancy, and absorbed water molecules, respectively (Figure 4(d)) [58]. When comparing all the spectra of each element between V-NCO/OPC and NCO/OPC, the ratios of Ni^{2+}/Ni^{3+} and Co^{2+}/Co^{3+} increased in V-NCO/OPC compared to those in NCO/OPC, indicating that M^{3+} ions were reduced to M^{2+} ions originating from the introduction of oxygen vacancies in the NCO lattice [59]. Furthermore, the O 1s spectrum of V-NCO/OPC exhibited decreased M-O bonding and an increased number of defect sites with oxygen vacancies compared to those of NCO/OPC, which also demonstrated the successful introduction of oxygen vacancies in the NCO lattice [60]. UV-vis analysis was conducted to investigate oxygen vacancies, comparing absorbance between bare NCO and V-NCO sheets without carbon. The lower absorbance in V-NCO sheets suggests the presence of oxygen vacancies affecting its structure and reducing bandgap energy compared to NCO sheets in Figure S8(a). Bandgap energies extrapolated from the linear part following the Tauc plot in Figure S8(b) were determined as 3.2/1.6 eV for NCO sheets and 2.9/1.4 eV for V-NCO sheets, which is evidence for the existence of oxygen vacancy in V-NCO [61]. To further demonstrate the existence of oxygen vacancies in the NCO lattice, an electron paramagnetic resonance (EPR) analysis was conducted. The EPR spectra shown in Figure S9 demonstrated that the signals in both samples with $g = 2.213$ could be assigned to paramagnetic oxygen vacancies. V-NCO/OPC exhibits a higher signal intensity at $g = 2.213$ than NCO/OPC, which verifies the existence of oxygen vacancies in V-NCO/OPC.

To demonstrate the effect of hybridization with an open porous structure of the carbon framework and oxygen vacancies in the NCO lattice on electrocatalytic activity, linear sweep voltammetry (LSV) measurements were carried out in an O_2-saturated alkaline electrolyte (0.1 M KOH). In the ORR LSV curves shown in Figure 5(a), V-NCO/OPC exhibited a higher onset potential ($E_{onset} = 0.96$ V) and half-wave potential ($E_{1/2} = 0.82$ V) than NCO/OPC (0.94 V (E_{onset}), 0.81 V ($E_{1/2}$)) and NCO/PC (0.93 V (E_{onset}), 0.77 V ($E_{1/2}$)). Although the onset and half-wave potential of V-NCO/OPC were still lower than those of the benchmark catalyst (Pt/C, 1.0 V (E_{onset}), 0.92 V ($E_{1/2}$)), the limited current density of V-NCO/OPC (4.72 mA cm^{-2}) was higher than that of Pt/C (4.57 mA cm^{-2}). Moreover, Tafel plots, which are the criteria for reaction kinetics, showed that V-NCO/OPC possessed the lowest Tafel slope (68 mV dec^{-1}) compared to NCO/OPC (81 mV dec^{-1}), NCO/PC (113 mV dec^{-1}), and Pt/C (99 mV dec^{-1}) (Figure 5(b)). The EIS experiments were carried out to explore catalytic kinetics (Figure S10). The EIS spectrum under ORR conditions revealed that the smaller charge transfer resistance (R_{ct}) observed in V-NCO/OPC and NCO/OPC, compared to NCO/PC, is attributed to the presence of macropores facilitating electrolyte transport. These results indicate the superior ORR activity and kinetics of V-NCO/OPC compared with those of the other samples. To further investigate this synergistic effect, the electrochemical surface area (ECSA) of each sample was compared using the double-layer capacitance (C_{dl}) values calculated by cyclic voltammetry (CV) measured in the non-Faraday region at various sweep rates (Figure S11). Based on the CV data of the prepared samples, the obtained C_{dl} value of V-NCO/OPC (21.8 mF cm^{-2}) was higher than those of NCO/OPC (18.1 mF cm^{-2}) and NCO/PC (1.7 mF cm^{-2}), which indicates that V-NCO/OPC

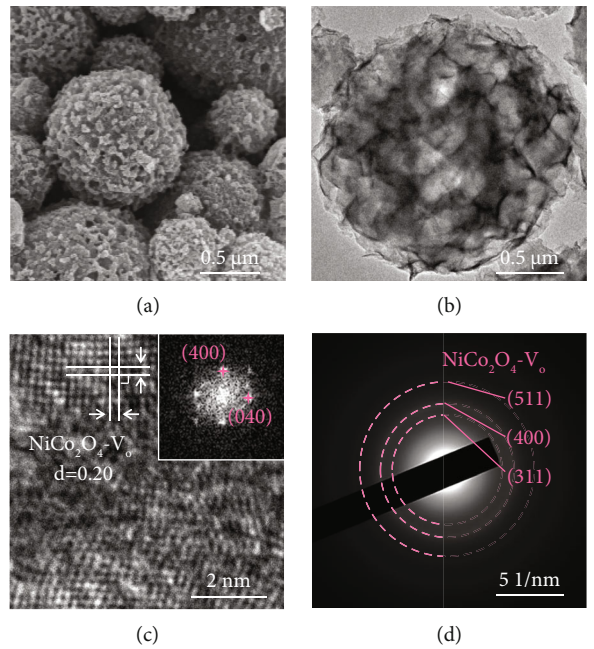

Figure 3: Morphologies and SAED pattern of V-NCO/OPC: (a) SEM image, (b) TEM image, (c) HR-TEM image (insert: fast Fourier transform electron diffraction pattern), and (d) SAED pattern.

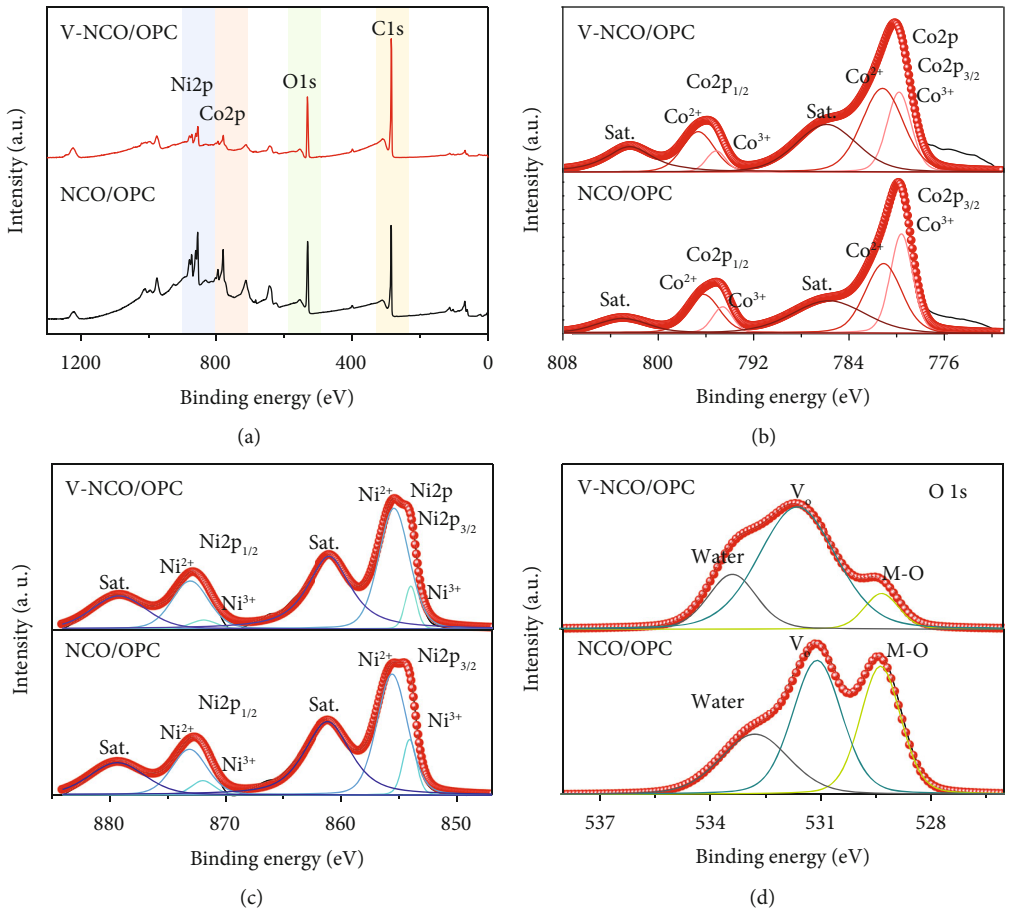

Figure 4: XPS spectra of V-NCO/OPC and NCO/OPC: (a) survey scan, (b) Co 2p, (c) Ni 2p, and (d) O 1s.

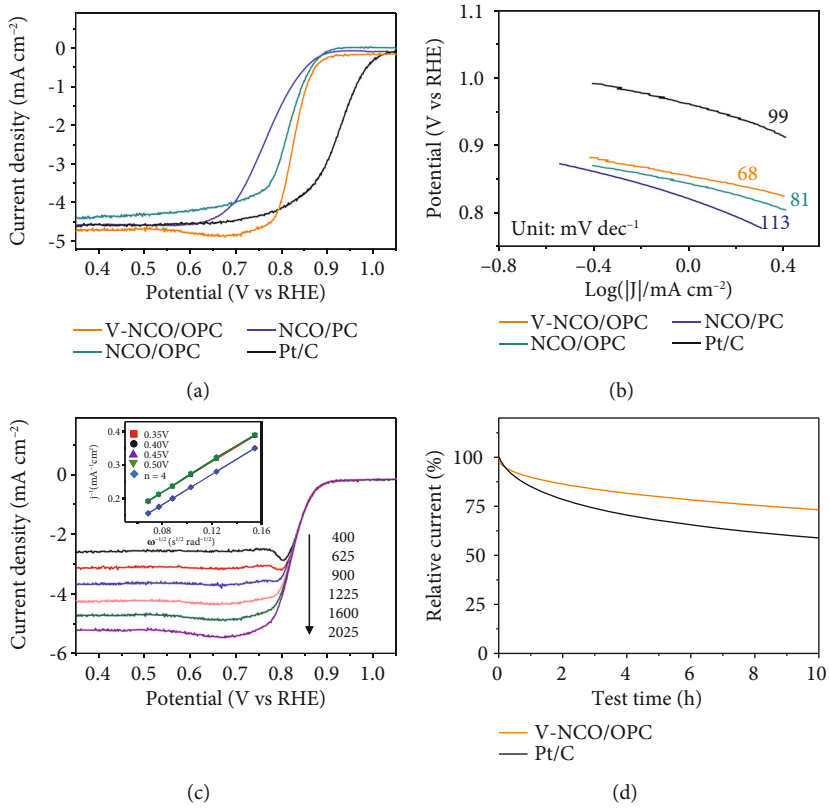

Figure 5: ORR characteristics of V-NCO/OPC, NCO/OPC, NCO/PC, and Pt/C: (a) LSV curves, (b) Tafel plots, (c) LSV curves at various rotating speeds (insert: corresponding K-L plots), and (d) chronoamperometric responses.

have numerous adsorption sites compared to other samples. To calculate the electron transfer number (n) for the ORR, LSV curves were measured at different rotation speeds from 400 to 2025 rpm, and the Koutecky-Levich (K-L) equation was applied using the LSV curves. As shown in Figure 5(c), all n values based on the K-L plots at each potential point are approximately 4, which is consistent with the four-electron transfer reactions during the ORR process. In ORR, since the durability of electrocatalysts is as important as activity and kinetics, the chronoamperometric responses of V-NCO/OPC and Pt/C were measured at the half-wave potential of each sample for 10 h. As shown in Figure 5(d), V-NCO/OPC maintained 73% of its initial current density, whereas Pt/C maintained only 58% of its initial current density, demonstrating the superior ORR durability of V-NCO/OPC compared to Pt/C. Furthermore, chronoamperometry was used to analyze the tolerance of methanol on the catalysts by adding 3 M methanol solution at 300 s in a 0.1 M oxygen-saturated KOH solution. While the commercial Pt/C catalyst exhibited a decline in performance due to oxidation with byproducts upon methanol addition, the V-NCO/OPC catalyst demonstrated remarkable durability under the same conditions, maintaining its performance (Figure S12). This result suggests the superior methanol tolerance property of V-NCO/OPC compared to Pt/C.

The OER characteristics of V-NCO/OPC, NCO/OPC, NCO/PC, and RuO_2 are shown in Figure 6. The LSV curves shown in Figure 6(a) revealed that V-NCO/OPC possessed a lower overpotential (402 mV) at 10 mA cm^{-2} than NCO/OPC (486 mV) and NCO/PC (516 mV), and higher than that of RuO_2 (360 mV). However, in terms of the OER kinetics, the Tafel slope of V-NCO/OPC is 195 mV dec^{-1}, which is lower than those of NCO/OPC (219 mV dec^{-1}), NCO/PC (222 mV dec^{-1}), and RuO_2 (204 mV dec^{-1}), as shown in Figure 6(b). Moreover, when the charge-transfer resistance (R_{ct}) was evaluated using electrochemical impedance spectroscopy (EIS), V-NCO/OPC exhibited the smallest R_{ct} among the samples in Figure 6(c). These results indicate that V-NCO/OPC has better OER activity than the other samples. The excellent bifunctional electrocatalytic activity of the V-NCO/OPC was triggered by the synergistic effect between the suitable pore structure of the carbon framework and the oxygen vacancies of NCO. The porous structure (micro/meso/macropores) of OPC can regulate the crystal growth to expose sufficient active sites, promote mass transport, and facilitate the detachment of the O_2 bubble-blocking surface of the active site. Moreover, oxygen vacancies in the NCO lattice modify the electronic structure of the NCO surface, which not only forms several active sites for adsorption but also enhances electrical conductivity.

Based on the superior bifunctional electrocatalytic properties of V-NCO/OPC, a homemade ZAB cell was assembled using V-NCO/OPC as an air cathode to demonstrate its practical application; its electrochemical properties are shown in Figure 7. A Pt/C+RuO_2 mixed electrocatalyst was used as the benchmark for comparison. The charge-

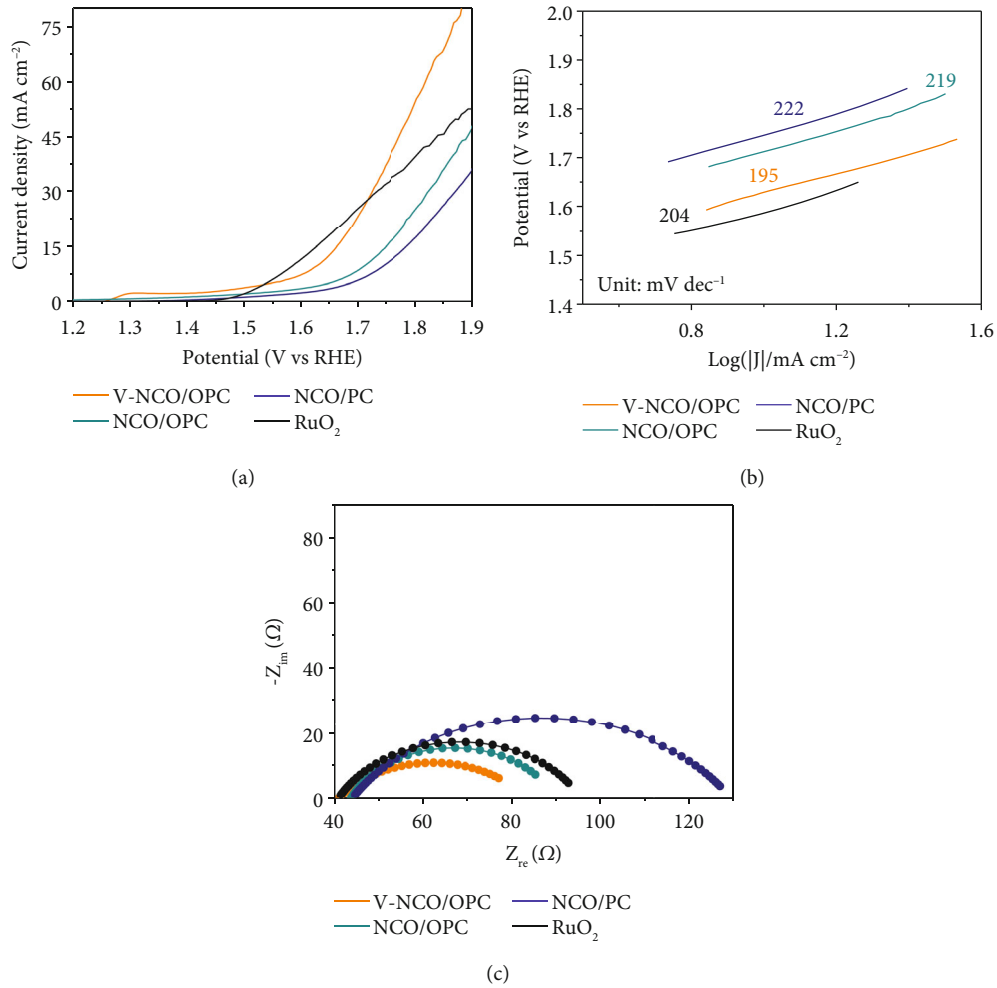

Figure 6: OER characteristics of V-NCO/OPC, NCO/OPC, NCO/PC, and RuO_2: (a) LSV curves, (b) Tafel plots, and (c) Nyquist plots of corresponding catalysts.

discharge polarization curves in Figure 7(a) revealed that the V-NCO/OPC electrode possessed a smaller voltage gap with a higher discharge voltage and lower charge voltage than the Pt/C+RuO_2 electrode, in agreement with the previous ORR and OER results. Moreover, as shown in Figure 7(b), V-NCO/OPC showed a peak power density of 154.9 mW cm^{-2} at a current density of 175.9 mA cm^{-2}, which was 1.3 times higher than that of Pt/C+RuO_2 (118.3 mW cm^{-2} at a current density of 123.0 mA cm^{-2}). The discharge-specific capacity, which is calculated based on the weight of the consumed zinc, is shown in Figure 7(c). At a current density of 10 mA cm^{-2}, V-NCO/OPC achieved a specific capacity of 758.8 mA h g_{Zn}^{-1} and a corresponding energy density of 940.9 W h kg_{Zn}^{-1}, which is better than Pt/C+RuO_2 (699.1 mA h g_{Zn}^{-1} and 894.8 W h kg_{Zn}^{-1}). In the rate capability shown in Figure 7(d), the discharge voltages of V-NCO/OPC were 1.31, 1.30, 1.28, 1.27, 1.25, 1,24, 1.23, and 1.22 V at 0.5, 1, 2, 4, 8, 10, and 20 mA cm^{-2}, respectively, which demonstrated superior reaction kinetics of V-NCO/OPC compared to Pt/C+RuO_2 even at high current density without sudden voltage drop for the ZAB system. The durability of the ZAB cathode was tested using galvanostatic charge and discharge measurements at 10 mA cm^{-2} with a 20 min period for one cycle (Figure 7(e)). The initial voltage gap between discharge (1.17 V) and charge (2.02 V) of V-NCO/OPC was 0.85 V, which altered to 0.95 V after 100 h of continuous cycling. In contrast, the voltage gap of Pt/C+RuO_2 was increased from 0.89 to 1.09 V at the initial cycle and after 100 h, respectively. Moreover, V-NCO/OPC exhibited long-term cycle stability for 250 h with a restricted increased voltage gap of 1.04 V, with 81% efficiency, as illustrated in Figure 7(f). To investigate the structural and chemical properties of V-NCO/OPC during the electrocatalytic process, ex situ SEM and XPS analyses were employed. SEM images of V-NCO/OPC shown in Figure S13 exhibited that the spherical shape was well-maintained after the discharge and recharge process, which suggests excellent structural stability. In the case of the XPS spectra shown in Figure S14, overall peak shifts from high to low binding energy were observed in the Ni 2p and Co 2p spectra. In the O 1s spectrum, several broad peaks corresponding to oxygen vacancies (V_o) and absorbed water were observed in a pristine state. However, the peak related to V_o bonding was increased after the recharge process, and the shape of the overall peaks became

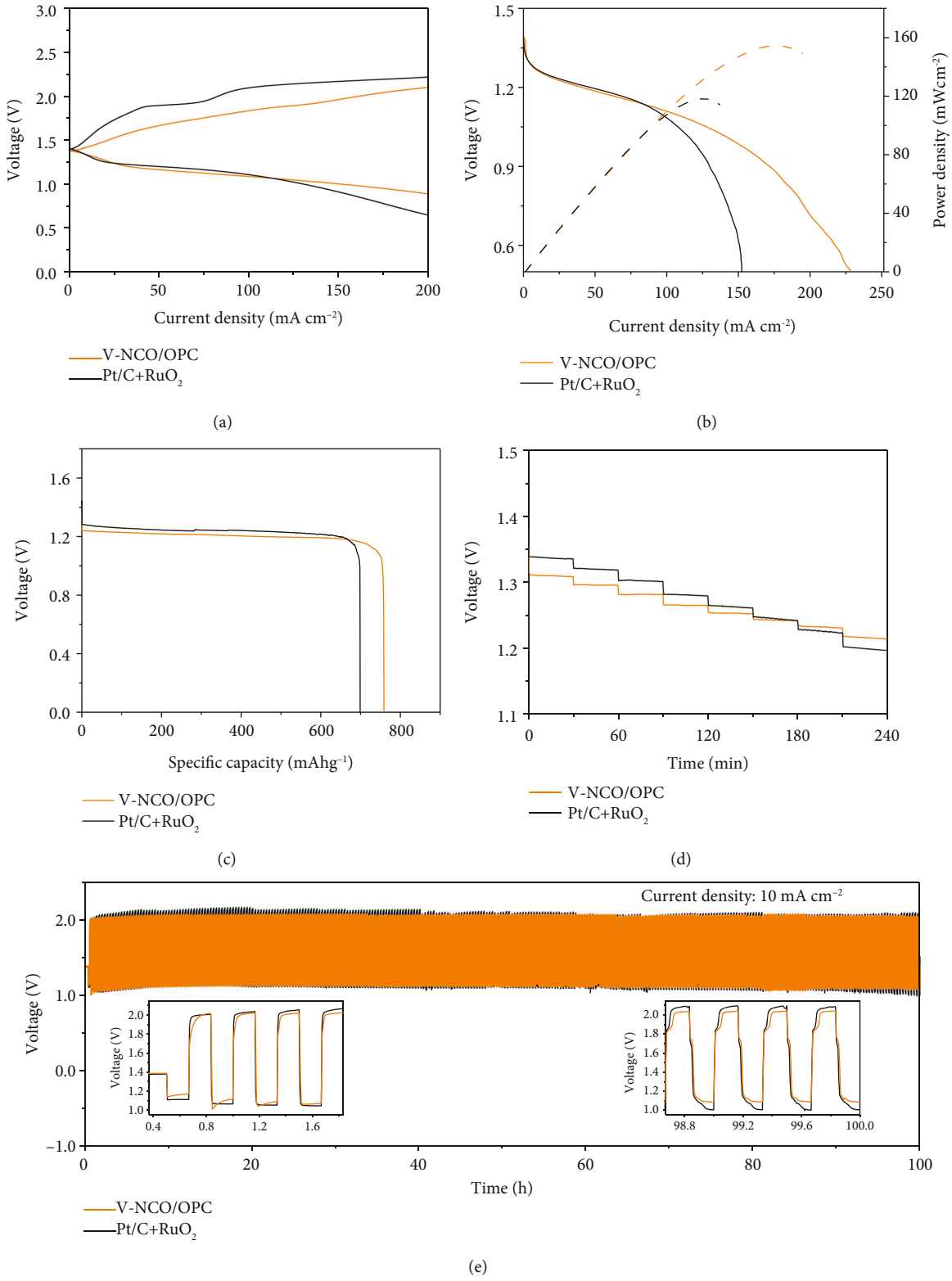

Figure 7: Continued.

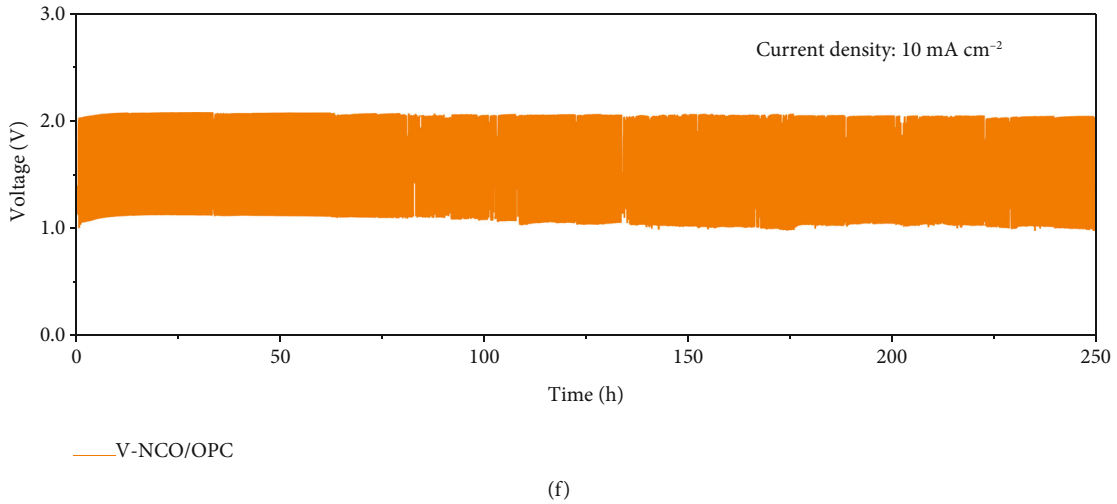

Figure 7: Electrochemical properties of V-NCO/OPC and Pt/C+RuO_2 for ZAB: (a) discharge and charge polarization curves, (b) polarization and corresponding power density curves, (c) specific energy densities, (d) rate performances, and (e, f) galvanostatic discharge and charge tests.

gradually sharper due to the dominance of V_o. These phenomena are attributed to the formation of carbon oxidation because of the high charging potential, which is consistent with results in previous literatures [62–64]. When comparing the ZAB performances of various composite materials comprised of NCO and carbonaceous materials reported in previous studies, V-NCO/OPC exhibited superior electrocatalytic properties compared to those of composite materials reported in the literatures (Table S1). Based on these results, V-NCO/OPC can be considered a superior ZAB cathode material compared to noble metal benchmarks in practical applications, owing to its pore structures, accelerating mass transfer, and large active sites from oxygen vacancies.

4. Conclusions

In summary, we developed open porous-structured carbon microspheres with a scaffold design containing micro/mesopores using an aerosol-based spray pyrolysis method. By using MgO and PS nanobeads as pore agents, OPC possessed micro/mesopores to regulate the crystal size when NCO nanosheets were loaded, as well as open macropores to facilitate mass transport and detachment of the O_2 bubble-blocking surface of the active site. Using the characteristics of OPC, ultrafine NCO nanosheets were uniformly decorated via a hydrothermal method and a subsequent oxidation process. The abundant micro/mesopores of OPC not only enable the uniform decoration of NCO nanosheets during the synthesis process but also inhibit their crystal growth. Moreover, to increase the number of active sites in the NCO nanosheets, oxygen vacancies were introduced into the NCO lattice via a partial reduction process using a $NaBH_4$ solution. Owing to the hybridization effect of each characteristic, V-NCO/OPC exhibited enhanced ORR and OER performances compared with noble-metal-based electrocatalysts. This study provides significant ideas for the fabrication of an efficient bifunctional oxygen electrocatalyst for ZAB based on pore design and defect introduction.

Data Availability

Data is available on request.

Conflicts of Interest

The authors declare that they have no conflicts of interest.

Authors' Contributions

Min Kim and Jeong Hoo Hong are the co-first authors of this paper.

Acknowledgments

This research was supported by the National Research Council of Science & Technology (NST) grant by the Korea government (MSIT) (No. CAP22082-100).

Supplementary Materials

Additional supporting information may be found online in the Supporting Information at the end of the article. Experimental Section (continued). Supplementary Figure S1: XRD pattern of Mg-OPC. Supplementary Figure S2: (a) N2 gas adsorption and desorption isotherm and (b) pore-size distribution of OPC and PC. Supplementary Figure S3: XRD patterns of NCO/OPC and NCO/PC. Supplementary Figure S4: morphologies and SAED pattern of NCO/PC: (a) SEM image, (b) TEM image, (c) HR-TEM image (insert: fast Fourier transform electron diffraction pattern), and (d) SAED pattern. Supplementary Figure S5: (a) N2 gas adsorption and desorption isotherm and (b) pore-size distribution of NCO/OPC and NCO/PC. Supplementary Figure S6: TG curves of NCO/OPC and NCO/PC. Supplementary Figure S7: XRD pattern

of V-NCO/OPC. Supplementary Figure S8: (a) UV-vis spectra and (b) Tauc plot of V-NCO and NCO. Supplementary Figure S9: EPR spectra of V-NCO/OPC and NCO/OPC. Supplementary Figure S10: the Nyquist plots of NCO/PC, NCO/OPC, V-NCO/OPC, and Pt/C under ORR condition. Supplementary Figure S11: cyclic voltammogram curves of (a) V-NCO/OPC, (b) NCO/OPC, and (c) NCO/PC, and (d) corresponding linear fitting of capacitive current. Supplementary Figure S12: methanol tolerance tests of V-NCO/OPC and Pt/C. Supplementary Figure S13: ex situ SEM images of V-NCO/OPC: (a) discharge and (b) recharge in ZABs. Supplementary Figure S14: ex situ XPS spectra of V-NCO/OPC: (a) Co 2p, (b) Ni 2p, and (c) O 1s. Supplementary Table S1: Zn-air battery performances of various composite electrocatalysts comprised of transition metal oxide and carbonaceous materials for air cathode reported in the previous studies. *(Supplementary Materials)*

References

[1] Y. Zhong, Z. Pan, X. Wang et al., "Hierarchical Co3O4Nano-Micro Arrays Featuring Superior Activity as Cathode in a Flexible and Rechargeable Zinc–Air Battery," *Advanced Science*, vol. 6, no. 11, article 1802243, 2019.

[2] X. Zhu, C. Hu, R. Amal, L. Dai, and X. Lu, "Heteroatom-doped carbon catalysts for zinc–air batteries: progress, mechanism, and opportunities," *Energy Environmental Science*, vol. 13, no. 12, pp. 4536–4563, 2020.

[3] T. Zhou, N. Zhang, C. Wu, and Y. Xie, "Surface/interface nanoengineering for rechargeable Zn–air batteries," *Energy Environmental Science*, vol. 13, no. 4, pp. 1132–1153, 2020.

[4] Z. Pan, J. Yang, W. Zang et al., "All-solid-state sponge-like squeezable zinc-air battery," *Energy Storage Materials*, vol. 23, pp. 375–382, 2019.

[5] M. Luo, W. Sun, B. B. Xu, H. Pan, and Y. Jiang, "Interface engineering of air electrocatalysts for rechargeable zinc–air batteries," *Advanced Energy Materials*, vol. 11, no. 4, article 2002762, 2021.

[6] C. Wang, J. Li, Z. Zhou et al., "Rechargeable zinc-air batteries with neutral electrolytes: recent advances, challenges, and prospects," *EnergyChem*, vol. 3, no. 4, article 100055, 2021.

[7] C. Chen, H. Su, L.-N. Lu et al., "Interfacing spinel NiCo2O4 and NiCo alloy derived N-doped carbon nanotubes for enhanced oxygen electrocatalysis," *Chemical Engineering Journal*, vol. 408, article 127814, 2021.

[8] S. J. Kim, J. H. Hong, J.-K. Lee, and Y. C. Kang, "Macroporous microspheres consisting of thickness-controlled bamboo-like CNTs and flower-like Co3O4nanoparticles as highly efficient bifunctional oxygen electrocatalysts for Zn–air batteries," *Journal of Materials Chemistry A*, vol. 9, no. 44, pp. 25160–25167, 2021.

[9] P. Rao, P. Cui, Z. Wei et al., "Integrated N-Co/carbon nanofiber cathode for highly efficient zinc–air batteries," *ACS Applied Materials & Interfaces*, vol. 11, no. 33, pp. 29708–29717, 2019.

[10] M. Chen, R. Abazari, S. Sanati et al., "Compositional engineering of HKUST-1/sulfidized NiMn-LDH on functionalized MWCNTs as remarkable bifunctional electrocatalysts for water splitting," *Carbon Energy*, vol. 5, no. 12, p. e459, 2023.

[11] M. S. Shim, J. H. Hong, and Y. C. Kang, "3D porous N and S Co-doped CNT microspheres with highly dispersed CoP nanoparticles: toward an efficient bifunctional electrocatalyst for Zn-air batteries," *International Journal of Energy Research*, vol. 2023, Article ID 5563539, 12 pages, 2023.

[12] Q. Lu, J. Yu, X. Zou et al., "Self-Catalyzed Growth of Co, N-Codoped CNTs on Carbon-Encased CoSxSurface: A Noble-Metal-Free Bifunctional Oxygen Electrocatalyst for Flexible Solid Zn–Air Batteries," *Advanced Functional Materials*, vol. 29, no. 38, article 1904481, 2019.

[13] A. Wang, C. Zhao, M. Yu, and W. Wang, "Trifunctional Co nanoparticle confined in defect-rich nitrogen-doped graphene for rechargeable Zn-air battery with a long lifetime," *Applied Catalysis B: Environmental*, vol. 281, article 119514, 2021.

[14] K. Ding, J. Hu, J. Luo et al., "Confined N-$CoSe_2$ active sites boost bifunctional oxygen electrocatalysis for rechargeable Zn–air batteries," *Nano Energy*, vol. 91, article 106675, 2022.

[15] M. Gopalakrishnan, W. Kao-Ian, M. Rittiruam et al., "3D hierarchical MOF-derived defect-rich NiFe spinel ferrite as a highly efficient electrocatalyst for oxygen redox reactions in zinc–air batteries," *ACS Applied Materials & Interfaces*, vol. 16, no. 9, pp. 11537–11551, 2024.

[16] D. Du, R. Zheng, M. He et al., "A-site cationic defects induced electronic structure regulation of $LaMnO_3$ perovskite boosts oxygen electrode reactions in aprotic lithium–oxygen batteries," *Energy Storage Materials*, vol. 43, pp. 293–304, 2021.

[17] J. Wang, R. Abazari, S. Sanati et al., "Water-stable fluorous metal–organic frameworks with open metal sites and amine groups for efficient urea electrocatalytic oxidation," *Small*, vol. 19, no. 43, article 2300673, 2023.

[18] J. H. Kim, M. Kim, J. H. Hong, J.-K. Lee, and Y. C. Kang, "Novel design and synthesis of multi-anionic Co(OH)Se with ZIF-67 derived porous carbon matrix as a bifunctional electrocatalyst for rechargeable Zn-air batteries," *Chemical Engineering Journal*, vol. 467, article 143359, 2023.

[19] K. Wu, L. Zhang, Y. Yuan et al., "An iron-decorated carbon aerogel for rechargeable flow and flexible Zn–air batteries," *Advanced Materials*, vol. 32, no. 32, article 2002292, 2020.

[20] M. Wang, C. Zhang, T. Meng et al., "Iron oxide and phosphide encapsulated within N, P-doped microporous carbon nanofibers as advanced tri-functional electrocatalyst toward oxygen reduction/evolution and hydrogen evolution reactions and zinc-air batteries," *Journal of Power Sources*, vol. 413, pp. 367–375, 2019.

[21] P. Rao, L. Yang, X. Wang, P. Cui, Y. Wang, and X. Zhao, "Lattice-compressed and N-doped Co nanoparticles to boost oxygen reduction reaction for zinc-air batteries," *Applied Surface Science*, vol. 525, article 146491, 2020.

[22] J. Liu, T. He, Q. Wang et al., "Confining ultrasmall bimetallic alloys in porous N–carbon for use as scalable and sustainable electrocatalysts for rechargeable Zn–air batteries," *Journal of Materials Chemistry A*, vol. 7, no. 20, pp. 12451–12456, 2019.

[23] R. Abazari, A. R. Amani-Ghadim, A. M. Slawin, C. L. Carpenter-Warren, and A. M. Kirillov, "Non-calcined layer-pillared Mn0.5Zn0.5bimetallic–organic framework as a promising electrocatalyst for oxygen evolution reaction," *Inorganic Chemistry*, vol. 61, no. 25, pp. 9514–9522, 2022.

[24] A. Worku, D. Ayele, and N. Habtu, "Recent advances and future perspectives in engineering of bifunctional electrocatalysts for rechargeable zinc–air batteries," *Materials Today Advances*, vol. 9, article 100116, 2021.

[25] T. Meng, B. Mao, and M. Cao, "In situ coupling of MnO and Co@N-doped graphite carbon derived from Prussian blue

analogous achieves high-performance reversible oxygen electrocatalysis for Zn–air batteries," *Inorganic Chemistry*, vol. 60, no. 14, pp. 10340–10349, 2021.

[26] M. Gopalakrishnan, M. Etesami, J. Theerthagiri et al., "Tailoring the MOF structurevialigand optimization afforded a dandelion flower like CoS/Co–Nx/CoNi/NiS catalyst to enhance the ORR/OER in zinc–air batteries," *Nanoscale*, vol. 14, no. 48, pp. 17908–17920, 2022.

[27] L. Wei, E. H. Ang, Y. Yang et al., "Recent advances of transition metal based bifunctional electrocatalysts for rechargeable zinc-air batteries," *Journal of Power Sources*, vol. 477, p. 228696, 2020.

[28] D. Ji, L. Fan, L. Tao et al., "The Kirkendall effect for engineering oxygen vacancy of hollow Co3O4nanoparticles toward high-performance portable zinc–air batteries," *Angewandte Chemie*, vol. 131, no. 39, pp. 13978–13982, 2019.

[29] T. Zhou, W. Xu, N. Zhang et al., "Ultrathin cobalt oxide layers as electrocatalysts for high-performance flexible Zn–air batteries," *Advanced Materials*, vol. 31, no. 15, article 1807468, 2019.

[30] X. Wang, Z. Liao, Y. Fu et al., "Confined growth of porous nitrogen-doped cobalt oxide nanoarrays as bifunctional oxygen electrocatalysts for rechargeable zinc–air batteries," *Energy Storage Materials*, vol. 26, pp. 157–164, 2020.

[31] Z. F. Huang, J. Wang, Y. Peng, C. Y. Jung, A. Fisher, and X. J. A. E. M. Wang, "Design of efficient bifunctional oxygen reduction/evolution electrocatalyst: recent advances and perspectives," *Advanced Energy Materials*, vol. 7, no. 23, article 1700S544, 2017.

[32] M. Wu, G. Zhang, H. Tong et al., "Cobalt (II) oxide nanosheets with rich oxygen vacancies as highly efficient bifunctional catalysts for ultra-stable rechargeable Zn-air flow battery," *Nano Energy*, vol. 79, article 105409, 2021.

[33] S. Chen, D. Huang, D. Liu et al., "Hollow and porous $NiCo_2O_4$ nanospheres for enhanced methanol oxidation reaction and oxygen reduction reaction by oxygen vacancies engineering," *Applied Catalysis B: Environmental*, vol. 291, article 120065, 2021.

[34] X. Liu, J. Wu, Z. Luo et al., "Co2P-assisted atomic Co–N4 active sites with a tailored electronic structure enabling efficient ORR/OER for rechargeable Zn–air batteries," *ACS Applied Materials & Interfaces*, vol. 15, no. 7, pp. 9240–9249, 2023.

[35] S. Chang, H. Zhang, and Z. Zhang, "FeCo alloy/N, S dual-doped carbon composite as a high-performance bifunctional catalyst in an advanced rechargeable zinc-air battery," *Journal of Energy Chemistry*, vol. 56, pp. 64–71, 2021.

[36] Y. Chen, I. Kone, Y. Gong et al., "Ultra-thin carbon nanosheets-assembled 3D hierarchically porous carbon for high performance zinc-air batteries," *Carbon*, vol. 152, pp. 325–334, 2019.

[37] J. H. Hong, J. K. Kim, D. S. Jung, and Y. C. Kang, "A synthetic strategy for graphitized carbon hollow nanospheres with nano-punched holes decorated with bimetallic selenide as efficient bifunctional electrocatalysts for rechargeable Li–O2batteries," *Journal of Materials Chemistry A*, vol. 11, no. 27, pp. 14997–15005, 2023.

[38] J. Y. Lee, G. D. Park, J. H. Kim, J. H. Hong, and Y. C. Kang, "Synthesis of three-dimensional Co/CoO/N-doped carbon nanotube composite for zinc air battery," *International Journal of Energy Research*, vol. 45, no. 11, pp. 16091–16101, 2021.

[39] W. Li, B. Liu, D. Liu et al., "Alloying Co species into ordered and interconnected macroporous carbon polyhedra for efficient oxygen reduction reaction in rechargeable zinc–air batteries," *Advanced Materials*, vol. 34, no. 17, article 2109605, 2022.

[40] S. Hu, W. Ni, D. Yang et al., "Fe_3O_4 nanoparticles encapsulated in single-atom Fe–N–C towards efficient oxygen reduction reaction: effect of the micro and macro pores," *Carbon*, vol. 162, pp. 245–255, 2020.

[41] M. Gopalakrishnan, A. Mohamad, M. Nguyen et al., "Recent advances in oxygen electrocatalysts based on tunable structural polymers," *Materials Today Chemistry*, vol. 23, article 100632, 2022.

[42] S. Liu, D. Ni, H.-F. Li, K. N. Hui, C.-Y. Ouyang, and S. C. Jun, "Effect of cation substitution on the pseudocapacitive performance of spinel cobaltite MCo_2O_4 (M= Mn, Ni, Cu, and Co)," *Journal of Materials Chemistry A*, vol. 6, no. 23, pp. 10674–10685, 2018.

[43] L. Wan, Z. Zhao, X. Chen et al., "Controlled synthesis of bifunctional $NiCo_2O_4$@ FeNi LDH core–shell nanoarray air electrodes for rechargeable zinc–air batteries," *ACS Sustainable Chemistry Engineering*, vol. 8, no. 30, pp. 11079–11087, 2020.

[44] H. Li, J. Wang, T. Tjardts et al., "Plasma-engineering of oxygen vacancies on NiCo2O4Nanowires with enhanced bifunctional electrocatalytic performance for rechargeable zinc-air battery," *Small*, no. article 2310660, 2024.

[45] J. Zhao, F.-W. Chen, X.-Y. Zhao, X.-J. Wang, Y.-P. Li, and F.-T. Li, "Self-composition of hierarchical core–shell-structured NiCo2O4@NiCo2O4microspheres with oxygen vacancies for efficient oxygen evolution electrocatalysis," *Energy & Fuels*, vol. 37, no. 23, pp. 18111–18119, 2023.

[46] H. Yuan, J. Li, W. Yang et al., "Oxygen vacancy-determined highly efficient oxygen reduction in NiCo2O4/hollow carbon spheres," *ACS Applied Materials & Interfaces*, vol. 10, no. 19, pp. 16410–16417, 2018.

[47] W. Liu, J. Bao, L. Xu et al., "$NiCo_2O_4$ ultrathin nanosheets with oxygen vacancies as bifunctional electrocatalysts for Zn-air battery," *Applied Surface Science*, vol. 478, pp. 552–559, 2019.

[48] Y. B. Kim, H. Y. Seo, K. H. Kim, J. S. Cho, Y. C. Kang, and G. D. Park, "Synthesis of iron sulfide nanocrystals encapsulated in highly porous carbon-coated CNT microsphere as anode materials for sodium-ion batteries," *Small*, vol. 20, no. article 2305686, 2023.

[49] J. H. Choi, J. W. Kang, H. Y. Koo, and Y. C. Kang, "Lithiophilic and conductive CuO-Cu_2O-Cu microspheres with controlled void structure via spray pyrolysis for improved lithium metal anode performance," *International Journal of Energy Research*, vol. 2023, Article ID 2200257, 15 pages, 2023.

[50] J. K. Kim, Y. Yoo, and Y. C. Kang, "Scalable green synthesis of hierarchically porous carbon microspheres by spray pyrolysis for high-performance supercapacitors," *Chemical Engineering Journal*, vol. 382, article 122805, 2020.

[51] N. Girija, S. S. Kuttan, T. Anusree, B. N. Nair, A. A. P. Mohamed, and U. N. S. J. A. A. N. M. Hareesh, "Nickel foam-supported NiCo2O4 urchin-shaped microparticles sheathed with NiCoO2 nanosheets as electrolyte-wettable electrodes for supercapacitors," *ACS Applied Nano Materials*, vol. 5, no. 10, pp. 14529–14539, 2022.

[52] J. Wang, Y. Zhang, J. Ye et al., "Facile synthesis of three-dimensional NiCo2O4with different morphology for supercapacitors," *RSC Advances*, vol. 6, no. 74, pp. 70077–70084, 2016.

[53] D. Li, H. Chen, G. Liu et al., "Porous nitrogen doped carbon sphere as high performance anode of sodium-ion battery," *Carbon*, vol. 94, pp. 888–894, 2015.

[54] Y. Ma, W. Shang, W. Yu et al., "Synthesis of ultrasmall NiCo2O4nanoparticle-decorated N-doped graphene nanosheets as an effective catalyst for Zn–air batteries," *Energy & Fuels*, vol. 35, no. 17, pp. 14188–14196, 2021.

[55] J. Liu, T. Chen, P. Jian, L. Wang, and X. Yan, "Hollow urchin-like $NiO/NiCo_2O_4$ heterostructures as highly efficient catalysts for selective oxidation of styrene," *Journal of Colloid Interface Science*, vol. 526, pp. 295–301, 2018.

[56] Z. Liu, C. Zhen, D. Xu et al., "Significantly enhanced photocurrent density in NiCo2O4/a-C/Si photoanode for water splitting," *Applied Surface Science*, vol. 529, article 147155, 2020.

[57] J. Zheng, X. Peng, Z. Xu, J. Gong, and Z. Wang, "Cationic defect engineering in spinel NiCo2O4for enhanced electrocatalytic oxygen evolution," *ACS Catalysis*, vol. 12, no. 16, pp. 10245–10254, 2022.

[58] J. Seong, A. M. Patil, S. B. Roy, J. Lee, and S. C. Jun, "N-doped oxygen vacancy-rich $NiCo_2O_4$ nanoarrays for supercapacitor and non-enzymatic glucose sensing," *International Journal of Energy Research*, vol. 46, no. 15, pp. 24501–24515, 2022.

[59] S. Pappu, K. Nanaji, S. Mandati, T. N. Rao, S. K. Martha, and S. V. Bulusu, "Cost-effective synthesis of electrodeposited NiCo2O4 nanosheets with induced oxygen vacancies: a highly efficient electrode material for hybrid supercapacitors," *Batteries & Supercaps*, vol. 3, no. 11, pp. 1209–1219, 2020.

[60] H. Tong, Q. Meng, J. Liu et al., "Cross-linked $NiCo_2O_4$ nanosheets with low crystallinity and rich oxygen vacancies for asymmetric supercapacitors," *Journal of Alloys Compounds*, vol. 822, article 153689, 2020.

[61] E. Umeshbabu, G. Rajeshkhanna, P. Justin, and G. R. Rao, "Magnetic, optical and electrocatalytic properties of urchin and sheaf-like $NiCo_2O_4$ nanostructures," *Materials Chemistry and Physics*, vol. 165, pp. 235–244, 2015.

[62] Y. He, W. Shang, M. Ni, Y. Huang, H. Zhao, and P. Tan, "In-situ observation of the gas evolution process on the air electrode of Zn-air batteries during charging," *Chemical Engineering Journal*, vol. 427, article 130862, 2022.

[63] W. Tang, J. Tang, K. Liao, and Z. Shao, "Self-reconstruction of highly active $NiCo_2O_4$ with triple-continuous transfer of electrons, ions, and oxygen for Zn-air batteries," *Chemical Engineering Journal*, vol. 455, article 140855, 2023.

[64] H. Park, B. H. Park, J. Choi et al., "Enhanced electrochemical properties and OER performances by Cu substitution in $NiCo_2O_4$ spinel structure," *Nanomaterials*, vol. 10, no. 9, p. 1727, 2020.